High Bandwidth Measurements of Auroral Langmuir Waves with Multiple Antennas

Chrystal Moser[1], James LaBelle[1], and Iver H. Cairns[2]

[1]Department of Physics and Astronomy, Dartmouth College, Hanover, NH, USA
[2]School of Physics, University of Sydney, Sydney, AU

Correspondence: Chrystal Moser (chrystal.s.moser@gmail.com)

Abstract. The High-Bandwidth Auroral Rocket (HIBAR) was launched from Poker Flat, Alaska on January 28, 2003 at 07:50 UT towards an apogee of 382 km in the night-side aurora. The flight was unique in having three high-frequency (HF) receivers using multiple antennas parallel and perpendicular to the ambient magnetic field, as well as very low frequency (VLF) receivers using antennas perpendicular to the magnetic field. These receivers observed five short-lived Langmuir wave bursts lasting from 0.1–0.2 s, consisting of a thin plasma line with frequencies in the range of 2470–2610 kHz that had an associated diffuse feature occurring 5–10 kHz above the plasma line. Both of these waves occurred slightly above the local plasma frequency with amplitudes between 1–100 μV/m. The ratio of the parallel to perpendicular components of the plasma line and diffuse feature were used to determine the angle of propagation of these waves with respect to the background magnetic field. These angles were found to be comparable to the theoretical Z-infinity angle that these waves would resonate at. The VLF receiver detected auroral hiss throughout the flight at 5–10 kHz, a frequency matching the difference between the plasma line and the diffuse feature. A dispersion solver, partially informed with measured electron distributions, and associated frequency- and wavevector-matching conditions were employed to determine if the diffuse features could be generated by a nonlinear wave-wave interaction of the plasma line with the lower frequency auroral hiss waves/lower-hybrid waves. The results show that this interpretation is plausible.

1 Introduction

Plasma waves generated at or near the local plasma frequency have been observed in the auroral ionosphere by satellites and rockets ever since there have been instruments capable of measuring them [review by Akbari et al. 2021]. These wave amplitudes can range from a few mV/m [McFadden et al., 1986] to greater than 1 V/m [Kintner et al., 1995] and have been observed in both under- ($f_{pe} < f_{ce}$) and over-dense ($f_{pe} > f_{ce}$) plasmas, where f_{pe} is the electron plasma frequency and f_{ce} is the electron cyclotron frequency [Beghin et al., 1989; McAdams et al. 1999]. Simultaneous observations of electron distribution functions and plasma waves have been reported by McFadden et al. [1987], Ergun et al. [1991a] and Beghin et al. [1989]. Langmuir waves can be generated both by electrons accelerated by parallel electric fields in the auroral acceleration region and scattered into a broad downgoing beam, or by concentrated parallel electron beams caused by Alfvénic acceleration. Beghin et al. [1989] also showed that frequency structures within the waves occur often in the auroral ionosphere, with an 80%

occurrence rate on the dayside and 60% on the nightside. More recent observations of Langmuir waves by the TRICE-1 (Twin Rockets to Investigate Cusp Electrodynamics) sounding rocket were reported by LaBelle et al. [2010], with modulations as low as 1 kHz and up to tens of kHz in an underdense plasma.

McAdams & LaBelle [1999] and Samara & LaBelle [2006] observed structured spectral peaks above the plasma frequency in High-Frequency (HF) spectrograms. The former dubbed these bursts “chirps", with amplitudes up to 1 mV/m relatively close to f_{pe}, and with similar amplitude diffuse waves occurring above the chirp signal. The latter reported several similar observations made by the SIERRA (Sounding of the Ion Energization Region: Resolving Ambiguities), PHAZE II (Physics of Auroral Zone Electrons), and RACE (Rocket Auroral Correlator Experiment) sounding rockets, all of which were in an overdense plasma. These were investigated theoretically by McAdams et al. [2000] who interpreted them as linear eigenmodes in pre-existing density structures. Similar Langmuir eigenmodes have subsequently been observed in the solar wind (Malaspina et al. 2008; Ergun et al. 2008).

Evidence for nonlinear processes has been reported, as recently reviewed by Akbari et al. [2021]. In addition to these various weak turbulence phenomena discussed above, there is evidence for strong turbulence phenomena in aurora, such as Langmuir cavitons [Akbari et al. 2013] as well as for electron and ion phase space holes (Ergun et al. 1998; Schamel et al. 2020; review by Akbari et al. 2021). Stasiewicz et al. [1996], using Freja satellite data, observed evidence of both parametric decay of a Langmuir wave into a lower hybrid (LH) and an oblique wave (L'), via the process $L \rightarrow L' + LH$, and scattering off an existing LH wave ($e.g., L + LH \rightarrow L'$), confirmed by Lizunov et al. [2001] and Khotyaintsev et al. [2001]. A model based on scattering of the plasma wave with an electrostatic whistler/lower hybrid wave is put forth as a plausible explanation for the modulations observed by Freja and SCIFER (Sounding of the Cusp Ion Fountain Energization Region) [Bonnell et al., 1997]. Cairns and Layden [2018] reviewed the decay process of generalized Langmuir waves into backscattered Langmuir waves and either ion acoustic waves or ion cyclotron waves, and showed, in a strongly magnetized plasma ($f_{pe} < f_{ce}$), the backscattered Langmuir wavenumber is greater than the initial Langmuir wavenumber, $k_{L'} > k_L$. Other nonlinear processes have been observed and studied in the auroral ionosphere involving Langmuir waves and whistler mode waves. Böhm et al. [1990] presented observation from two sounding rockets of intense Langmuir and whistler waves and showed they were associated with Alfvén waves. This process was shown to theoretically feasible through the parametric decay of Langmuir waves into whistler (W) and Alfvén electromagnetic ion-cyclotron (EMIC) waves (A), ($L \rightarrow W + A$) [Chian et al., 1994; Lopes and Chian 1996]. This theory could also be relevant to the observations of EMIC waves by the Auroral Turbulence sounding rocket reported by Lund and LaBelle [1997], who reviewed Langmuir turbulence in the auroral ionosphere induced by electron beams instabilities and ion density irregularities that result in the parametric decay of Langmuir waves into secondary Langmuir waves and ion acoustic waves, $k_L \rightarrow k_{L'} + k_s$.

McFadden et al. [1986] measured both parallel and perpendicular components of the electric field, observing Langmuir waves with larger parallel components such that $k_{||} > k_{\perp}$, that were coincident with unstable parallel electron distributions. Colpitts and LaBelle [2008] performed a Monte Carlo simulation of the Langmuir and Z-mode waves and showed their electric fields are preferentially parallel, becoming more perpendicular as the frequencies increased towards the UH frequency as expected. Dombrowski et al. [2012] used the unique 3-D data set from TRICE-1 to determine the intensity of the electric field for Langmuir waves and shows their parallel components are more than two times larger than their perpendicular components.

The High-Bandwidth Auroral Rocket (HiBAR) was one in a series of sounding rockets equipped with the telemetry capable of measuring high frequencies waves in detail. Uniquely, it achieved these measurements in both the parallel and perpendicular direction with respect to the background magnetic field, which allows for the identity of the wave mode (e.g., parallel propagating Langmuir wave or perpendicularly-propagating upper hybrid mode) and the direction of propagation of the different waves to be determined and compared with theory. Its goal was to measure waves generated by intense beams of electron precipitating down the magnetic field at high latitudes in the F-region of the ionosphere, where $f_{pe} < f_{ce}$. Previously, Samara et al. [2004] analyzed UH waves from HIBAR at the condition $f_{UH} = 2f_{ce}$, where f_{UH} is the upper hybrid (UH) frequency, the source of auroral roar emissions seen at ground level [review by LaBelle and Treumann 2002]. This report presents observations by the HIBAR mission of Langmuir wave bursts near f_{pe}, with a region of diffuse waves occurring at a frequencies 5-15kHz above the plasma bursts, as well as low frequency whistler mode hiss occurring between 5–15 kHz. The wave events are observed in the overdense regime. Using a wave dispersion solver to determine the normal modes of the waves and the growth rates for the normal modes, we will show these waves could plausibly be generated by a wave-wave interaction of the Langmuir wave with low frequency waves in the Lower-Hybrid mode.

2 Data Presentation

HIBAR was launched from Poker Flat, Alaska, on January 28, 2003, at 07:50 UT into active pre-midnight aurora, reaching an apogee of 382 km. The geomagnetic field was strongly perturbed, exhibiting a sequence of 50-100 nT magnetic bays in the north-south component, the first of which coincided with the rocket launch, indicating that an expansion phase or pseudo breakup was in progress. Its payload included a Langmuir probe, particle detectors, and DC, VLF and HF electric field receivers. HIBAR was one in a series of rockets with a high telemetry rate to measure waves with frequencies up to 5 MHz, allowing observations of detailed structure of high frequency waves in the lower ionosphere, such as Langmuir and Upper-Hybrid (UH) waves. The rocket's spin axis was aligned to within 5 degrees of the background magnetic field, with a spin rate of 0.95 Hz. For wave measurements, the rocket included two radial booms oriented perpendicular to one another and three axial booms, one along the axis of the rocket protruding from the front deck, and two mounted on the ends of the radial booms (see Figure 1).

The unique feature of HIBAR was the large number of HF telemetry links. Among these, two were dedicated to measurements of components of HF wave electric fields up to 5 MHz: the perpendicular electric field used probes x_1 and x_3, located 2.5 m apart oriented perpendicular to the rocket axis, and the parallel electric field used probes x_1 and x_2, located 0.28 m apart and oriented along the rocket axis. Voltage differences between these probe pairs, amplified and filtered, modulated dedicated transmissions from rocket to ground station. An automatic gain control (AGC) was used to optimize dynamic range. The AGC level was transmitted as a separate PCM link and combined with the HF signal in post analysis. Four electrostatic analyzers

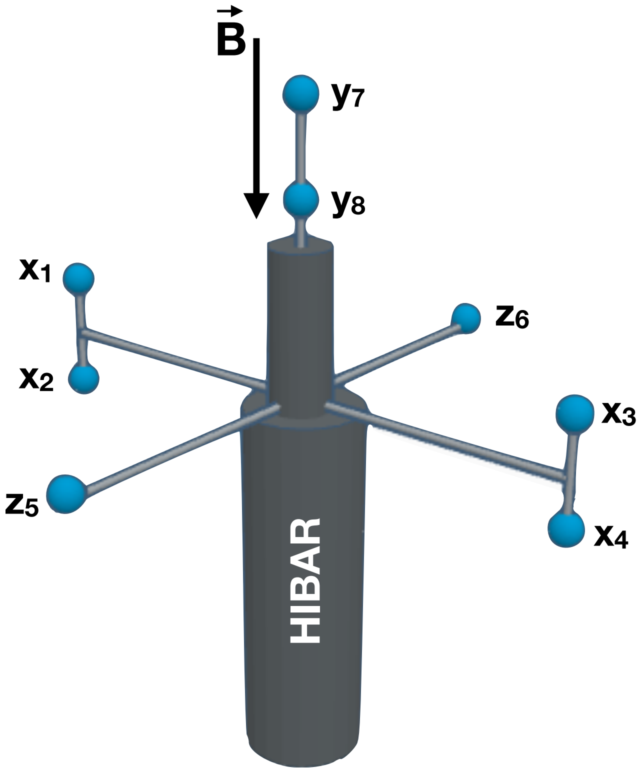

Figure 1. Diagram of the HIBAR rocket showing approximate antenna orientations with respect to the background magnetic field. (note: the labeling of the probes has no connection to Cartesian coordinates.)

(ESA) measured ion and electron energies from 70 eV to 19 keV at 8 pitch angles from 0°–180°, sweeping through the energy steps every 45 milliseconds.

Figure 2a–b shows HF spectrograms from both perpendicular and parallel antennas covering 07:54:13–07:54:33 UT (253–273 s) flight time and the altitude range to ∼364–374 km, one of the intervals when Langmuir waves were observed. Figure 2c–d show data for a slightly later interval, 07:55:49–07:56:09 UT (349–369 s), corresponding to 377–370 km altitude, which also contains Langmuir waves. As usual, plasma noise is enhanced in the band between f_{pe} and f_{UH}, so that the local plasma frequency can be seen as lower cutoffs in both the spectrograms between 2400 and 2700 kHz, and the upper-hybrid frequency can be seen as an upper cutoff in the perpendicular spectrograms between 2800 and 3000 kHz. During these two time intervals, HIBAR encountered seven short-lived wave bursts near f_{pe} that last from $\sim 0.1 - 0.2$ s, five of which had a diffuse band occurring 5-10kHz above a narrow plasma wave line (see Figure 4) and well below the upper hybrid band above 2800 kHz. These five events are labeled in Figure 2 by their respective times (in seconds after launch), occurring at 07:54:20, 07:54:22,

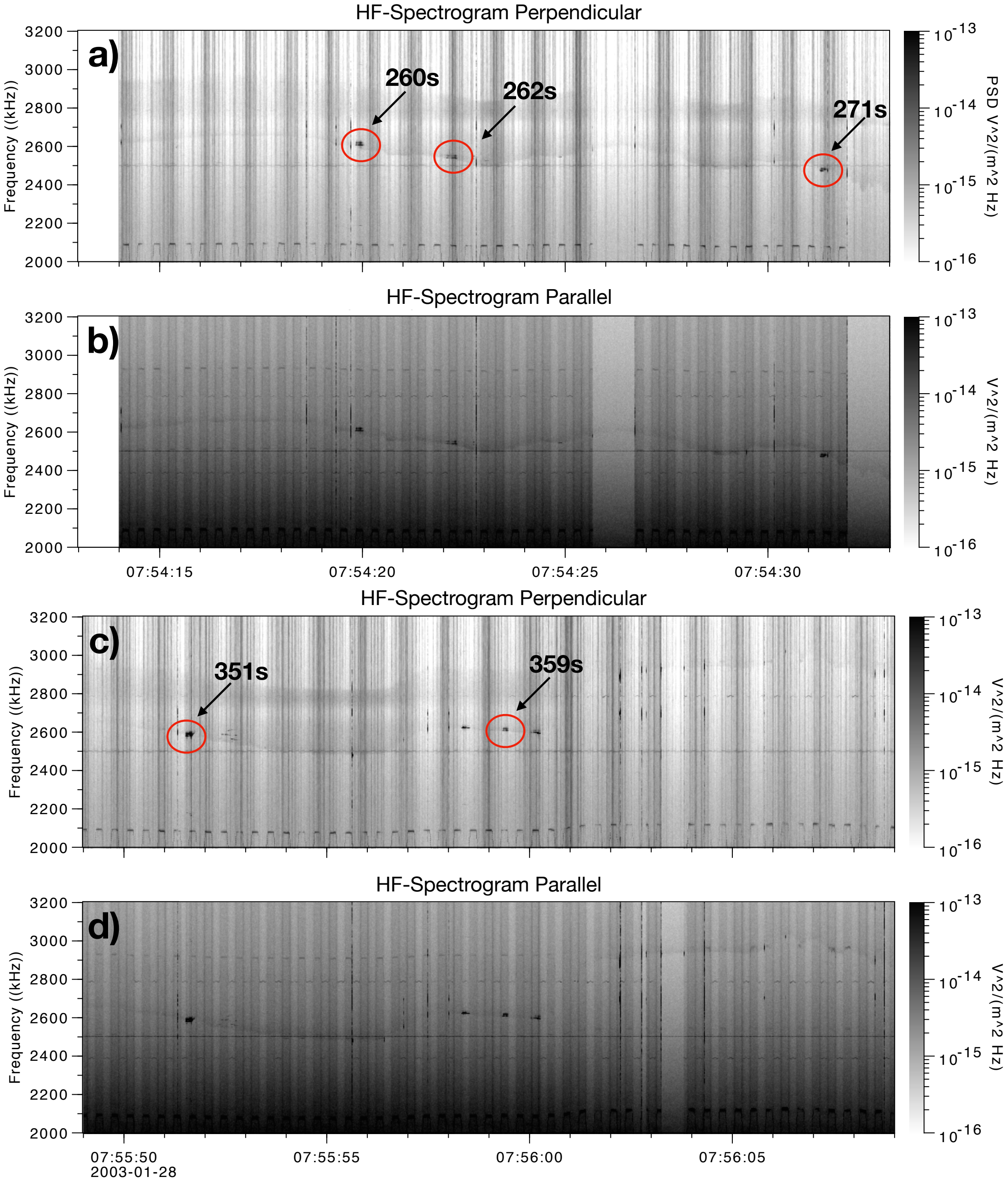

Figure 2. 2000-3200 kHz spectrograms of perpendicular (upper panels a & c) and parallel (lower panels b & d) HF electric fields for two time intervals during the HIBAR rocket flight: 07:54:18–07:54:33 UT and 07:55:49–07:36:04 UT, showing the plasma frequency cutoff as a lower bound in the perpendicular and parallel spectrograms, and the upper-hybrid frequency cutoff as an upper bound in the perpendicular spectrograms. Red circles indicate five Langmuir wave bursts used for detailed study.

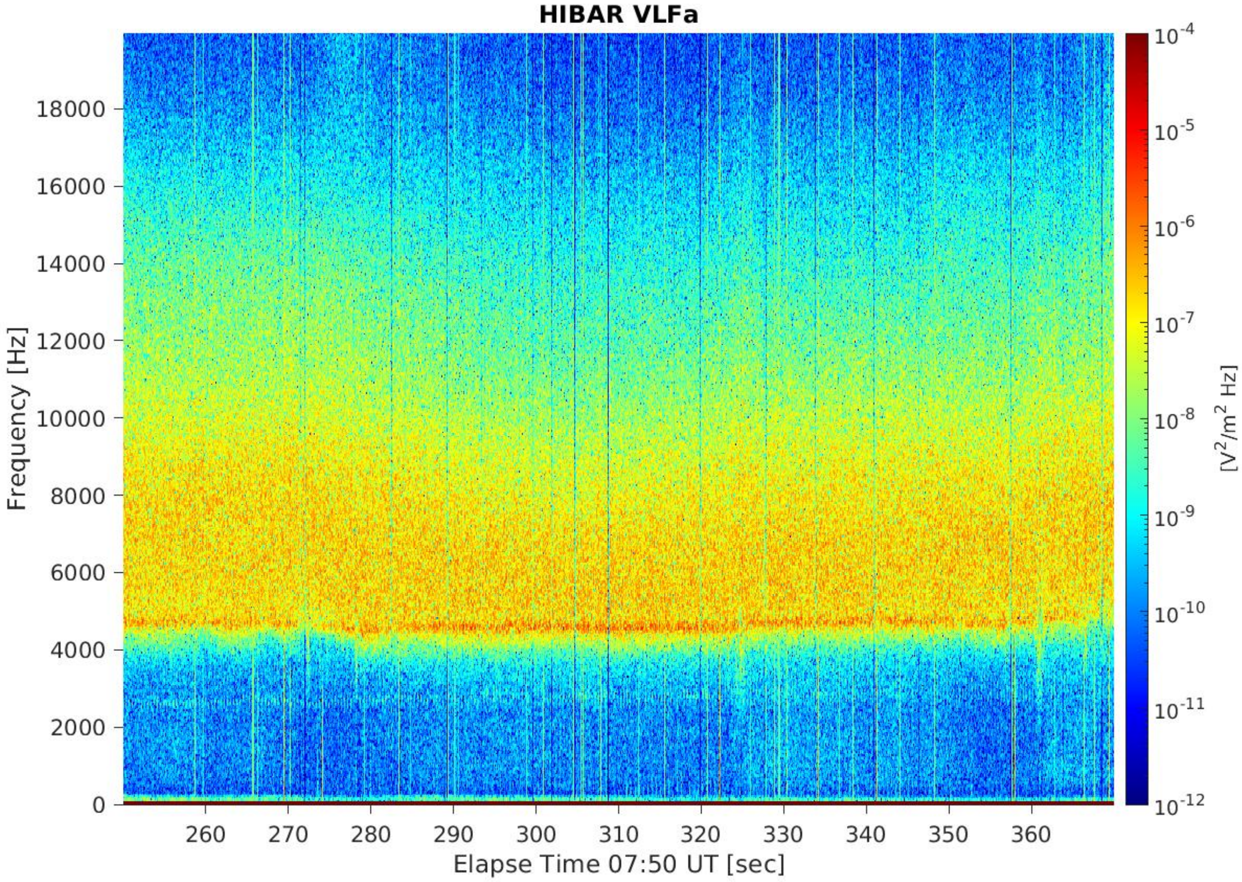

Figure 3. Frequency-Power spectrogram of the HIBAR VLF wave data from 0-20 kHz and 07:54:10–07:56:10 UT (250–370 s) showing the broadband diffuse whistler mode waves, and a slightly enhanced power band at ∼5 kHz corresponding to probable LH waves.

07:54:32 in Figure 2a–b and 07:55:51 and 07:55:59 UT in Figure 2c–d. For the entirety of both intervals in Figure 2, HIBAR is in overdense plasma ($f_{pe} > f_{ce}$).

Figure 3 shows the Very-Low Frequency (VLF) data in a frequency-time spectrogram for the interval when the Langmuir wave bursts are seen, between 07:54:10–07:56:10 UT (250–370 s) and ∼360–380 km. There is a broadband enhancement of the whistler mode waves between 4–15 kHz, with a small band of slightly more enhanced waves at approximately 5 kHz, believed to be near the LH frequency because it acts as a cutoff to the whistler mode. These waves were measured with a separate perpendicular antenna, oriented 90° to the antennas used to measured the HF waves, using probes z5 and z6 in Figure 1.

Figure 4 shows enhanced spectrograms of five selected Langmuir wave events observed by both the parallel and perpendicular HF antenna labeled 260s, 262s, 271s, 351s, and 359s in Figure 2. These events include a thin, intense plasma line just

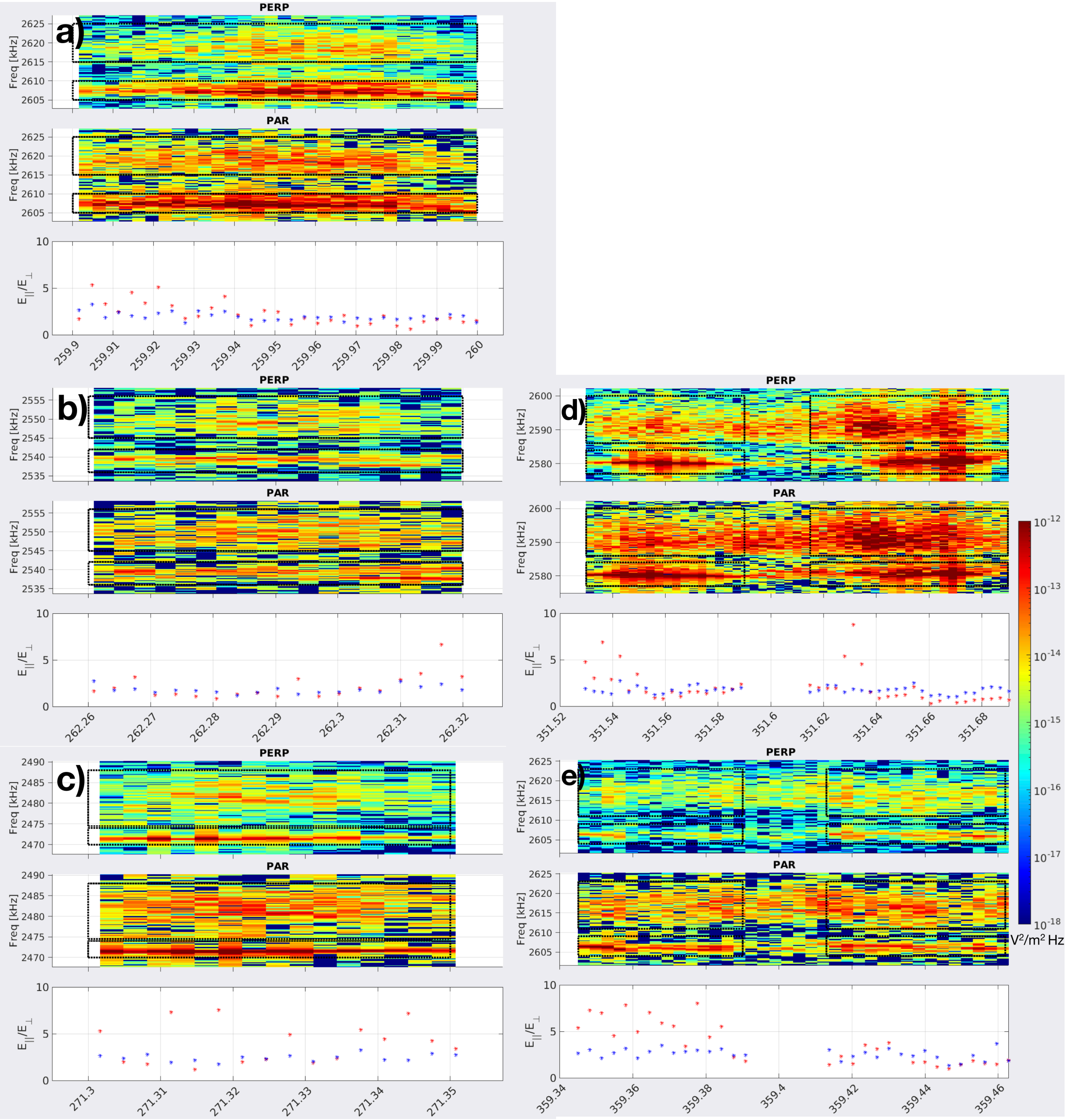

Figure 4. Enhanced plots of the five Langmuir bursts indicated in Figure 2, presented in time order, each comprised of a narrow band plasma line and a broadband diffuse feature with ∼5–15 kHz higher frequency. The top panels in each plot are from the perpendicular antenna, the middle panels are from the parallel antenna, and the bottom panels are the parallel to perpendicular ratios of the amplitudes of the plasma peaks (red) and the diffuse feature (blue).

above the plasma frequency cutoff and a less intense band of waves above the plasma line, referred to as the diffuse feature. Other plasma line events occurred during HIBAR; however, these did not include the diffuse waves, and therefore were not considered in this study. Obtaining absolute units for the electric fields of these features requires combining the AGC voltage data with the raw HF waveform data. These values were then divided by the length of the respective booms to obtain electric fields in V/m, under the assumption, discussed below, that the wavelength is longer than the probe separation.

Black boxes in each spectrogram in Figure 4 outline time and frequency intervals used to calculated average intensities of the plasma line and diffuse features of each event. Figure 5 shows details of this calculation for a selected event, shown in Figure 4a as occurring at 259.9–260.0 s. Separately for both the parallel and perpendicular spectra, the background power spectral density level was determined for each event by computing the average spectral density over a slightly higher frequency range, as indicated by the upper black box spanning 2640–2660 kHz in Figure 5a–b. The background interval was selected separately and was slightly different for each of the other four events shown in Figure 4. For each event, a spectrum was produced by subtracting this average background power spectral density from each spectrum. Figure 5c shows example spectra after this subtraction, for both perpendicular (blue trace) and parallel (red trace) for the time indicated by a red vertical line in Figure 5a–b. This was done because the background noise, either from the instrument or from the environment, was significantly different between the two antennas, and would have effected the ratio of the electric fields. It was removed for a more accurate estimate of the ratio of the parallel to perpendicular electric fields.

The average intensity of each feature for each antenna is determined by integrating the appropriate spectrum over the frequency range of the feature, bounded by the vertical dashed line in Figure 5c, corresponding to the black boxes in Figure 4 and Figure 5a–b. In the case of the selected event shown in Figure 5, the intensity is 7.8×10^{-9} V^2/m^2 (4.6×10^{-10} V^2/m^2) for the plasma line with the parallel (perpendicular) antenna, and 3.3×10^{-10} V^2/m^2 (5.2×10^{-11} V^2/m^2) for the diffuse feature with the parallel (perpendicular) antenna. These numbers combine to imply that $E_{||}/E_{\perp}$ is 2.3 ± 1.2 for the plasma wave and 2.0 ± 0.4 for the diffuse wave when averaged over the whole interval of the event shown in Figure 5, with the standard deviation specified.

Bottom panels of each section of Figure 4 display $E_{||}/E_{\perp}$ ratios for both the plasma line (red points) and diffuse feature (blue points) as a function of time through the five selected events. For the plasma line, the variation in this ratio is noteworthy: it seems to toggle between a fairly high ratio, around five, and a low ratio near unity. There is no obvious feature in the spectrograms mirroring these changes in the polarization state, leading us to investigate the theoretical or instrumental reason for this unexpected result (discussed below). Because of this non-stationarity of the polarization, $E_{||}/E_{\perp}$ ratios averaged over the entire event may be misleading. Table 1 summarizes the polarization measurements of each event shown in Figure 3. The table has seven rows because two of the events, at 351 and 359 s, have been split into two events, as indicated by the black boxes in Figures 4d–e, because they each have a gap in the plasma line suggesting they may be two events in close proximity. Table 1 tabulates both the average $E_{||}/E_{\perp}$ ratio, which may be misleading as discussed above, the maximum $E_{||}/E_{\perp}$ ratio defined as the average of the highest three measured ratios, and the minimum $E_{||}/E_{\perp}$ ratio defined as the average of the lowest three measured ratios for consistency. Uncertainty estimations are based on standard deviations associated with the averages taken in obtaining each $E_{||}/E_{\perp}$ value.

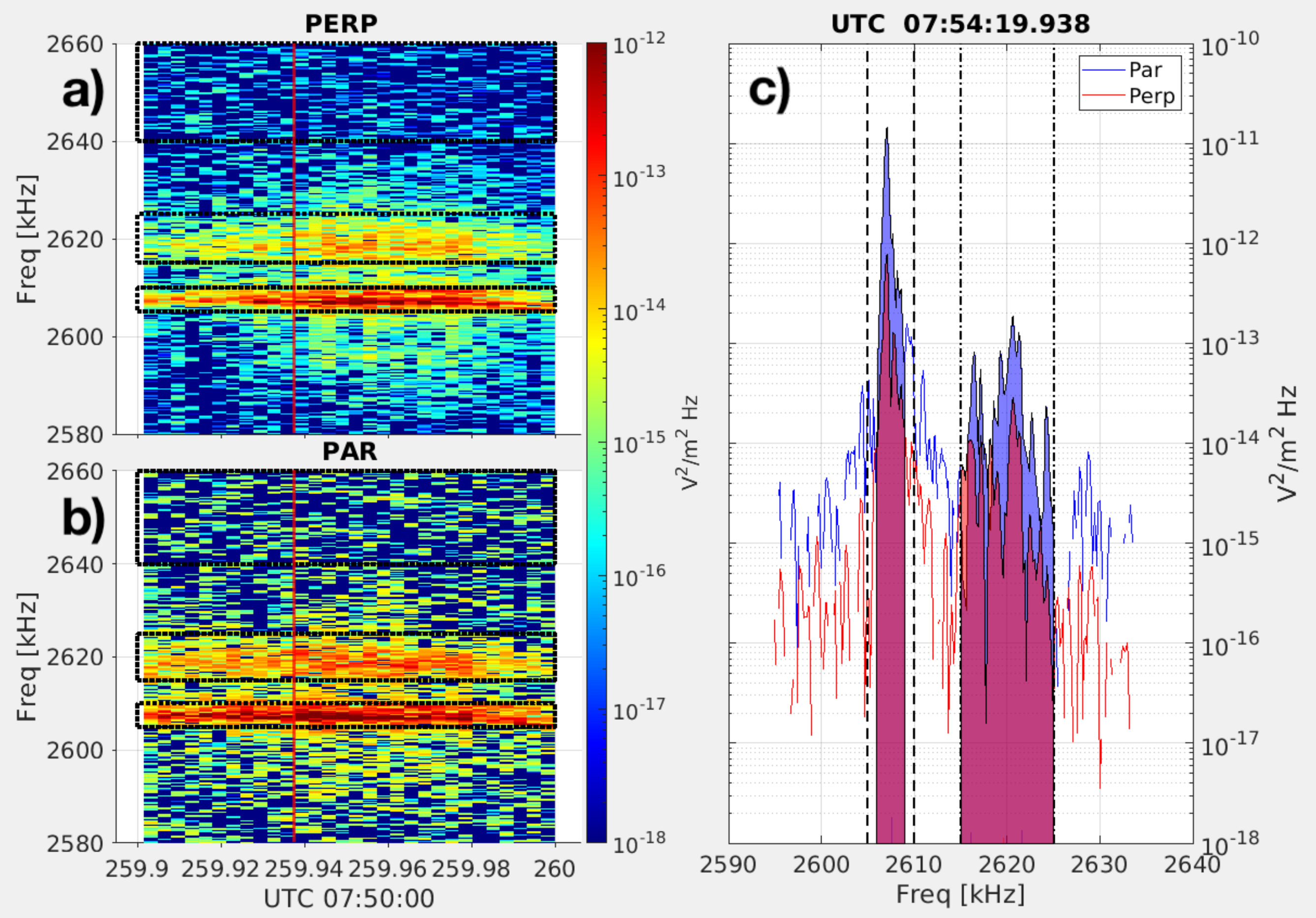

Figure 5. (a) Perpendicular and (b) parallel spectrograms for the Langmuir bursts labeled 260s in Figure 2 and shown in Figure 4a. Black boxes indicate the frequency-time ranges used to define the plasma line, diffuse feature, and background level. (c) Selected spectrum with background noise subtracted, occurring at the time highlighted as a red vertical line in panels (a) and (b), showing the power spectral density of the parallel waves (blue) versus the perpendicular waves (red).

Table 1. Mean ratios of $E_{||}/E_{\perp}$, maximum $E_{||}/E_{\perp}$ defined as the mean of the three largest ratios for each event, and minimum $E_{||}/E_{\perp}$ defined as the mean of the three smallest ratios for each event with their standard deviations for both the plasma line (f_p) and the diffuse feature (f_{diff}), for Langmuir bursts defined in Figures 2–4. Event's 351 and 359 were split into 2 separate events because of the gap in the plasma line in the middle of the event interval.

Event Time [s]	$E_{\|\|}/E_{\perp}$ Mean ratio		$E_{\|\|}/E_{\perp}$ Max Ratio		$E_{\|\|}/E_{\perp}$ Min Ratio	
	f_p	f_{diff}	f_p	f_{diff}	f_p	f_{diff}
260	2.25 ± 1.23	1.97 ± 0.44	5.01 ± 0.40	2.84 ± 0.37	0.86 ± 0.19	1.35 ± 0.05
262	2.15 ± 1.39	1.83 ± 0.43	4.49 ± 1.90	2.63 ± 0.19	1.01 ± 0.13	1.36 ± 0.16
271	3.97 ± 2.17	2.46 ± 0.39	7.38 ± 0.20	3.01 ± 0.24	1.63 ± 0.37	1.92 ± 0.15
351–1	2.45 ± 1.65	1.84 ± 0.40	5.71 ± 1.10	2.50 ± 0.25	0.95 ± 0.12	1.32 ± 0.07
351–2	1.84 ± 1.96	1.71 ± 0.38	6.38 ± 2.26	2.35 ± 0.14	0.41 ± 0.09	1.07 ± 0.07
359–1	5.41 ± 1.91	2.78 ± 0.38	7.73 ± 0.38	3.28 ± 0.21	2.50 ± 0.84	2.23 ± 0.17
359–2	2.02 ± 0.84	2.38 ± 0.65	3.50 ± 0.34	3.32 ± 0.33	1.22 ± 0.21	1.51 ± 0.18

Table 2. The resulting angles θ from Equation (3) for the mean and maximum ratios defined in Table 1 for both the plasma line (θ_p) and diffuse feature (θ_{diff}).

	$E_{\vert\vert}/E_{\perp}$	Mean ratio	$E_{\vert\vert}/E_{\perp}$	Max Ratio
Event Time [s]	θ_p	θ_{diff}	θ_p	θ_{diff}
260	24°	27°	11°	19°
262	25°	28°	13°	21°
271	14°	22°	8°	18°
351–1	22°	29°	10°	22°
351–2	28°	30°	9°	23°
359–1	10°	20°	7°	17°
359–2	26°	20°	16°	17°

3 Discussion

We now use the ratios of $E_{||}$ to $E_{\perp}$ to determine the wave modes and directions of propagation of the waves, by comparing the observations with theory. In order to determine what type of waves are being observed, whether they are quasi-parallel Langmuir waves or if they are oblique Z-mode waves, the ratios of the parallel to perpendicular electric field are used to determine the angle of wave propagation and compared to plasma theory. The mean $E_{||}/E_{\perp}$ ratios in Table 1 for the plasma line range from 1.8 to 5.4 and average 2.9, in approximate agreement with previous measurements which had generally lower time resolution. For example, McFadden et al. [1986] reported ratios ranging from 3-10. As noted by McFadden et al. [1986], wavelength as well as polarization can affect the measured ratio $E_{||}/E_{\perp}$. In the case of HIBAR, electrons measured with the ESA had relatively high energy, in the range 10-20 keV. For a plasma frequency of $\sim$2600 kHz, this implies Langmuir waves with parallel wavelengths of $\sim$23–32 m would resonate with the electron distribution measured by HIBAR. Assuming that the standard electron beam Langmuir wave instability for electrons with these energies gives rise to the plasma line implies that the wavelength should exceed the probe separations which were of order 0.3 m for the parallel measurement. The perpendicular measurement used longer boom separation, 3.0 m, but the measured $E_{||}/E_{\perp}$ ratio suggests that measurement is also in the long-wavelength regime. This means that the wave polarization should be the dominant effect determining the measured $E_{||}/E_{\perp}$ ratio for the plasma line.

McFadden et al. [1986] also point out that the perpendicular component of the wave may be underestimated in the measurement by a factor cosϕ, where ϕ is the angle between the perpendicular electric field boom and the instantaneous perpendicular wavevector, assuming that the wave has a distinct perpendicular wavevector rather than being distributed over a range of wavevectors during the time of measurement. In the latter case, the perpendicular electric field will be underestimated by a smaller factor. These considerations raise the question of whether the observed bimodal distributions of $E_{||}/E_{\perp}$, seemingly toggling between high values ≥ 5 and low values near unity, result from variations in the angle between the perpendicular boom and the wave vector projected into the plane perpendicular to $\boldsymbol{B}$, rather than variations in the fundamental polarization of the waves. In principle, it is impossible to distinguish these two possibilities since both types of time variation of the wave vector could equally well produce the observed $E_{||}/E_{\perp}$ ratios. It is possible to infer, however, that if the angle between the perpendicular boom and the wave vector projected on the plane perpendicular to $\boldsymbol{B}$ is stationary, the mere rotation of the booms cannot explain the observed variations in $E_{||}/E_{\perp}$ (since the observed variations do not appear to repeat at the spin period).

An attempt to determine the angle of the perpendicular wavevector to the antennas orientation results in poor fits to the observed time series of $E_{||}/E_{\perp}$ (not shown), as the observed data have zero correlation or, in some cases, the exact opposite correlation, to the expected trend based on the fit equations. The time variations in the measured $E_{||}/E_{\perp}$ suggest that either some aspect of the polarization, the $E_{||}/E_{\perp}$ ratio itself, or the angle of the $E_{\perp}$ vector changes on sub-second timescales, giving rise to variations in the observed value of $E_{||}/E_{\perp}$, or the waves are distributed over some peculiar range of angles such that the rocket spin produces this effect through variation of the angle between the boom and the projection of the electric field vector into the plane perpendicular to $\boldsymbol{B}$. Either way, one may safely infer that $k_{||}$ exceeds $k_{\perp}$ for these waves, as expected for Langmuir waves close to the plasma frequency or sufficiently oblique Z-mode waves (also known as the generalized Langmuir wave [Willes and Cairns, 2000] which is the Langmuir wave and upper hybrid wave in the limits of parallel and perpendicular propagation, respectively, and the oblique Z-modes in between).

It is worth noting, however, that Langmuir waves driven in the relatively unmagnetized solar wind by electron beams with energies of order 100 keV and above can naturally have $E_{||}/E_{\perp} < 1$ [Graham and Cairns, 2013a; Malaspina and Ergun, 2008]. Because there are some observations where the perpendicular component is larger than the parallel component, it is worth determining the theoretical energies these observations would require, and to compare them to the measured energies of the particles at the time of the events. Theoretically, this situation involves wave growth driven by the electron beam on or at least near the z-mode portion of the generalized Langmuir mode, corresponding to frequencies very near and below f_{pe} [Willes and Cairns, 2000]. The relevant condition on the wavenumbers is

$$k_w^* \lambda_D = \frac{V_e}{c} \left[cos^2\theta + \frac{\omega_{pe}}{\omega_{ce}} \right]^{1/2} \text{ or} \tag{1}$$

$$k^* = \frac{\omega_{pe}}{c} \left[cos^2\theta + \frac{\omega_{pe}}{\omega_{ce}} \right]^{1/2} \tag{2}$$

where k^* is the wavenumber, ω_{pe} is the electron plasma frequency, c is the speed of light, θ is the angle of the wavevector with respect to the background magnetic field, and ω_{ce} is the electron cyclotron frequency. In the HiBAR situation, where $\omega_{pe}/\omega_{ce} \approx 2$, this requires wavenumbers on the order of 0.1 m^{-1}. Ignoring semi-relativistic and magnetization effects, the corresponding speeds are $v = \omega_{pe}/k^* \approx 0.5c$. The corresponding energies are ~70 keV, between the energies of ~10 - 100 keV considered standard for the auroral ionosphere, but beyond the energy range that the electrostatic analyzer could measure. Accordingly at this time, we seek an explanation in terms of slower electron beams.

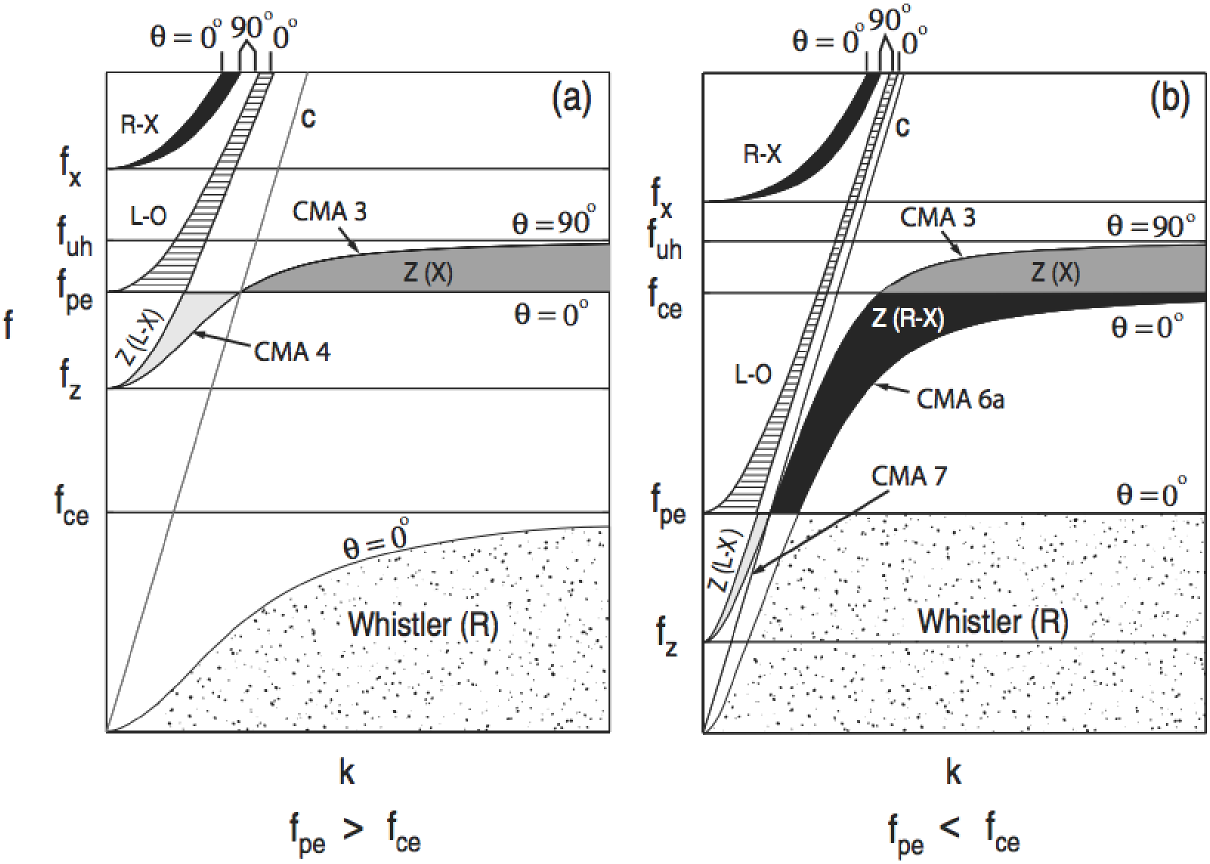

Figure 6. Dispersion relations for the different wave modes for an overdense ($f_{pe} > f_{ce}$) and underdense ($f_{pe} < f_{ce}$) plasma, adapted from Benson et al. [2006]. The Z-mode cutoff above the plasma frequency for an overdense plasma increases from 0 to $\frac{\pi}{2}$.

3.1 Electric Field Component Ratios

Theory also suggests that as waves increase in frequency away from the local plasma frequency, they should become more perpendicular, decreasing the ratio of parallel to perpendicular electric field (see Figure 6). This prediction is confirmed in this study (see Tables 1 and 2), where the ratios $E_{||}/E_{\perp}$ of the plasma lines exceed those of the diffuse feature that occurs at higher frequencies. This is true for the total average over each event interval ($E_{||} \approx (2 \text{ to } 5)E_{\perp}$ for the plasma line and $E_{||} \approx 2E_{\perp}$ for the diffuse feature), and for the average max ratio between the two waves ($E_{||} \approx (4 \text{ to } 8)E_{\perp}$ for the plasma line and $E_{||} \approx 3E_{\perp}$ for the diffuse feature). In the extreme case, waves near f_{UH} reported by Samara et al. [2004] have very small $E_{||}/E_{\perp}$ ratios with an average of 0.05 (see Figure 2 of Samara et al., 2004).

Table 3. Plasma frequency cutoff (f_{pe}), plasma line frequency (f_p), diffuse feature frequency range (f_{diff}), and resonant z-mode oblique angles, θ_p and θ_{diff}, calculated from equation (4), for Langmuir bursts labeled in Figures 2–4.

Event Time [s]	Plasma Cutoff f_{pe} [kHz]	f_p [kHz]	f_{diff} [kHz]	θ_p [deg]	θ_{diff} [deg]
260	2586	2607	2615-2625	12	14-17
262	2525	2540	2545-2556	10	12-15
271	2460	2471	2475-2488	4	7-11
351	2575	2580	2586-2600	8	11-15
359	2600	2606	2611-2623	9	11-14

From the ratios in Table 1 the angle of wave propagation can be calculated using simple geometry by assuming the electric field amplitude ratio is proportional to the wavenumber ratio ($E_{||}/E_{\perp} = k_{||}/k_{\perp}$), as expected for electrostatic waves, where the angle with respect to the magnetic field, θ, is given by

$$\theta = 90^\circ - \tan^{-1}\left(\frac{E_{||}}{E_{\perp}}\right). \tag{3}$$

Table 2 shows calculations of these angles for both the total average ratio and the max average ratio, and for both the plasma line and the diffuse feature.

The unique capability of the HIBAR mission to measure both the parallel and perpendicular components of the electric field means the propagation angles of waves with respect the background magnetic field can be compared to the expected values from plasma theory. Because these waves occur slightly above the plasma frequency cutoff in the overdense plasma ($f_{pe} > f_{ce}$), they fall into the Z-mode region (see Figure 6 adapted from Benson et al. 2006). In this region, for waves with phase velocities less than c, the waves can experience resonance referred to as the upper oblique resonance given by Benson et al. (2006)

$$f_{ZI} = \frac{1}{\sqrt{2}}\left[f_{UH}^2 + (f_{UH}^4 - 4f_{ce}^2 f_{pe}^2 cos^2\theta)^{\frac{1}{2}}\right]^{\frac{1}{2}}. \tag{4}$$

The frequency that waves can resonate in this region, Z-infinity f_{ZI}, depends on the local electron plasma frequency f_{pe}, the electron cyclotron frequency $f_{ce} \approx 1350$ kHz, and the angle that the wave propagates at with respect to the background magnetic field, θ. In the limit $\theta \to \frac{\pi}{2}$, $f_{ZI} = f_{UH}$, and in the limit $\theta \to 0$, $f_{ZI} = \max[f_{pe}, f_{ce}]$. Table 3 lists the frequencies for the plasma cutoff (f_{pe}), the plasma line (f_p, assumed to be f_{ZI}), and the range of the diffuse feature (f_{diff}) for each wave burst, labeled by when they occurred in seconds post launch, along with the calculated oblique angle of the Z-infinity resonance. The angles calculated from equation (4) agree fairly well with the angles determined from the electric field ratios in equation (3). These angles agree better with the angles calculated from the average of the max power ratios than the average over all power ratios for each event for both the plasma line and diffuse feature, consistent with the non-stationary aspect of these waves. This suggests these waves are resonating at the Z-infinity resonance angle.

Table 4. Parameters used for computing dispersion surfaces in WHAMP associated with Langmuir bursts labeled in Figures 2–4.

Event Time [s]	B [nT]	n [cm^{-3}]	$T_{\|\|}$ [eV]
260	48402	82953	0.2
262	48345	79337	0.2
271	48202	75128	0.2
351	48074	81294	0.2
359	48380	83854	0.2

3.2 Non-Linear 3-Wave Interaction

The plasma lines and corresponding diffuse features last for identical time intervals. This raises the possibility that the diffuse features are generated by wave-wave interactions of the plasma lines with lower frequency waves. HIBAR was equipped with a very-low frequency (VLF) receiver that measured waves from 0– 20 kHz, which showed a consistent whistler mode hiss for the times when the HF waves are observed (e.g. Figure 3). The whistler hiss ranges from 5-15 kHz and has wave electric fields on the order of tens of mV/m. The broad range of whistler waves surrounding the rocket could interact with the plasma line to generate the broad range that the diffuse wave exhibits.

To test the plausibility of the wave-wave interaction hypothesis, a dispersion solver, Wave in Homogeneous Anisotropic Multicomponent Plasma (WHAMP, Rönnmark 1982), was employed to calculate surfaces corresponding to the normal modes in the plasma that might participate in the wave-wave interaction: the Langmuir-Upper Hybrid (UH) and the Whistler-Lower Hybrid (LH) surfaces. WHAMP requires user defined input parameters for the plasma environment, including the magnetic field strength, number of particle species and their respective densities and temperatures. Table 4 lists the parameter values used for modeling each HIBAR event. The two species used were electrons and oxygen ions, which are the dominant ions at low altitudes, and each were represented by a basic Maxwellian distribution. The densities were determined from the plasma frequency cutoff, and the magnetic field from the magnetometer on board the rocket. Temperatures were taken to be 0.2 eV, typical of auroral F-region, and assumed to be isotropic.

Figure 7 shows the WHAMP surfaces for each of the 5 events, where the x and y axes are the perpendicular and parallel wavenumbers normalized to the electron gyroradius, and the z axis is the wave frequency normalized to the electron gyrofrequency. For the Langmuir-UH surface, in the parallel wavenumber limit the frequency equals the electron plasma frequency and in the perpendicular limit the frequency equals the upper-hybrid frequency. For small wavenumbers ($\rho_{||}k_\perp < 10^{-2}$) this surface corresponds to the Z-mode (cf Willes and Cairns, 2000). On the Whistler-LH surface, in the large parallel wavenumber limit ($k_{||} \gg k_\perp$) the frequencies approach the electron cyclotron frequency. The LH surface is found at near perpendicular propagation ($k_\perp \gg k_{||}$). At oblique angles near parallel to $\boldsymbol{B}$ ($k_{||} > k_\perp$), the surface corresponds to the whistler mode.

For each Langmuir-UH surface in Figure 7 the black (white) line represents the values of $k_{||}/k_\perp$ inferred from the average of the maximum $E_{||}/E_\perp$ ratios listed in Table 1 for the plasma lines (diffuse features). The widths of these lines are determined by the standard deviations of the ratio. The corresponding plasma line and diffuse feature frequencies are plotted as patches of yellow and pink, respectively. For each plasma line and diffuse feature, where the line for $k_{||}/k_{\perp}$ intersects the patch for the observed wave frequency is the locus of allowed frequencies and wavevectors on the normal mode surface. The red line represents where $\rho_{||}k_{||}$ corresponds to 20 keV, the maximum electron energy observed by the electrostatic analyzer during the time of the events, via the relationship $k = \omega\sqrt{m_e/2E}$. If the plasma lines were generated by parallel Landau resonance with these high energy electrons, then where the black plasma line ratio and yellow frequency patch intersect should be close to the condition represented by the red line. This occurs for events labeled 260s, 271s, 351s-1, 351s-2, and 359s-1.

To generate the highlighted surface sections in Figure 7, these waves are assumed to be electrostatic, that is the ratio of the parallel to perpendicular components of the wavevector are assumed to be equal to the ratio corresponding electric field components. The theoretical ratios of the electric field computed by the WHAMP dispersion code for the points on the Langmuir/UH surface highlighted in Figure 7 match the observed values (Table 1), within 10-25$\%$. This suggests that although the waves are not purely electrostatic, the values are close enough to the measured values that the assumption that $k_{||}/k_{\perp} = E_{||}/E_{\perp}$ is reasonable.

Assuming a nonlinear 3-wave interaction is responsible for the generation of the diffuse feature, the possible third wave should be connected through the wavevector matching condition, $\boldsymbol{k}_3 = \boldsymbol{k}_{\text{diff}} - \boldsymbol{k}_p$, which results from momentum conservation in the interaction [e.g., Tsytovich, 1970; Melrose, 1980; Cairns, 1987, 1988; Cairns and Layden, 2018; Moser et al., 2021]. The wavenumbers $\boldsymbol{k}_p$ and $\boldsymbol{k}_{\text{diff}}$ are determined by the two intersections of wavenumber ratio (black and white) and frequency matching (pink and yellow) on the Langmuir-UH surface. The dark blue patch on the whistler/LH surface in each panel of Figure 7 represents the range of k-vectors on the whistler/LH surface that satisfies this condition. The three modes must also obey the frequency matching condition, $\omega_3 = \omega_{\text{diff}} - \omega_p$. Light blue points within the region of possible k-vectors for the third wave represent modes that also satisfy the frequency matching condition. All events have a possible third wave that could interact with the plasma line to generate the diffuse feature. In each case Figure 7 suggest the third wave is well-described as a whistler/LH wave.

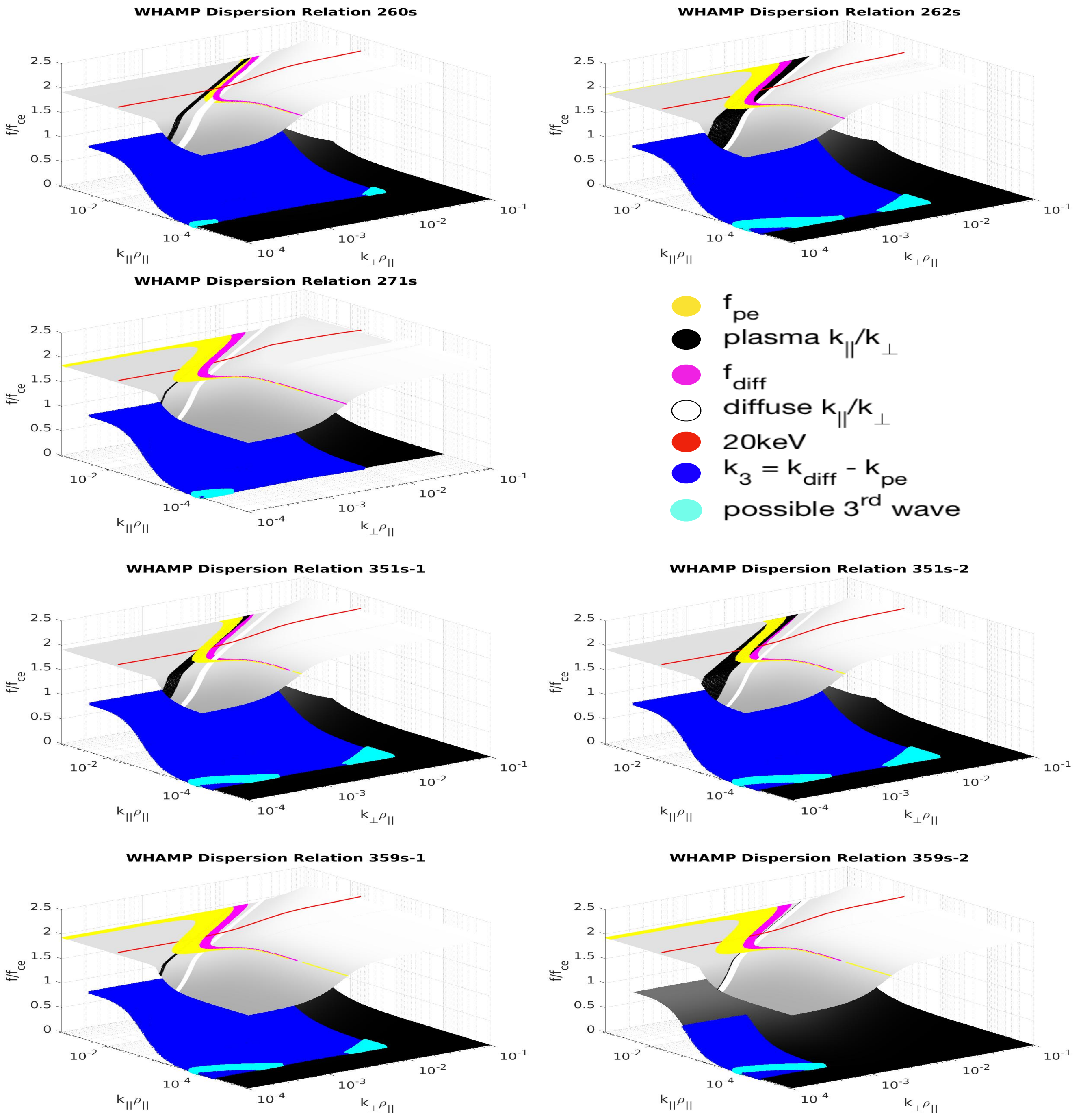

Figure 7. WHAMP dispersion surfaces for Langmuir bursts labeled in Figures 2–4, with $k_{||}/k_{\perp}$ ratios inferred from the maximum $E_{||}/E_{\perp}$ in Table 1 plotted as black for the plasma line and white for the diffuse feature. The yellow and pink areas indicate where the surface matches the frequency of the plasma line and diffuse feature, respectively. Where these intersect defines the range of possible k-vectors for each wave. Assuming wave-wave interaction, kinematic equations imply a range of k-vectors for the possible third wave plotted in dark blue on the whistler/LH surface, and the matching frequency of the third wave plotted in light blue.

These waves were produced by some form of energy exchange of particles with the plasma environment, and the electron and ion data were examined to determine the source of these waves. Similar to the analysis of growth rates in Moser et al. [2021b], the electron and ion distribution functions are needed to determine growth rates on the two dispersion surfaces produced by WHAMP. The measured electron distribution for the time 07:54:19.907 UT is shown in Figure 8a, for event labeled 260s, with a model of the high energy electron distribution in Figure 8b produced by the WHAMP parameters: temperature, density, magnetic field strength, drift velocity, and anisotropy. The x-axis represents the parallel velocity, where the positive axis is along the background magnetic field and the negative axis is anti parallel to the magnetic field. The y-axis represents the velocity perpendicular to the background magnetic field. The high energy electrons, while not the most prominent feature in the electron distribution, were used to model the distribution because equation (2) suggests these waves are produced by particles with higher energies. It should be noted that the electron ESA could only measure electrons with energies below 20 keV, which limits the range of electron energies that can be modeled.

Figure 8c shows the whistler/LH mode surface produced in WHAMP with growth rates from the model distribution in Figure 8b for the event labeled 260s. The model distribution has a parallel temperature $\mathrm{T}_{||}$ = 50 eV, density $n = 1$ cm^{-3}, magnetic field $\boldsymbol{B} = 48402.0$ nT, a drift velocity $v_D = 5u_{||}$, and an anisotropy ratio of $\mathrm{T}_{||}/\mathrm{T}_{\perp}$ = 5. There are two areas of growth that are of interest, at low $\mathrm{k}_{\perp}$ and high $\mathrm{k}_{\perp}$, where the frequency and wavenumber matching conditions are met. At low $\mathrm{k}_{\perp}$ the growth rate are $\sim 10^{-8}$ Hz, smaller than the growth rates at higher $\mathrm{k}_{\perp}$ of $\sim 10^{-6}$ Hz, but both are too low to likely produce these waves. However, the true unstable distributions may not be captured with the particle instruments, even with proper energy range and resolution, because unstable distributions rapidly stabilize. So while the growth rates with the observed distribution are low, they show that growth should occur and could increase to non-linear levels with a more suitable electron distribution. The areas of larger growth at higher frequencies near $k_{\perp}\rho_{||} = 10^{-2}$ on the whistler mode surface are potentially generating the whistler modes waves observed in the HF spectra at frequencies between about 50 and 350 kHz. The model electron distribution in Figure 8 was also used to generate the Langmuir/z mode surface (not shown) and found to produce no instabilities at frequencies and wavenumbers that correspond to the modes in Figure 7.

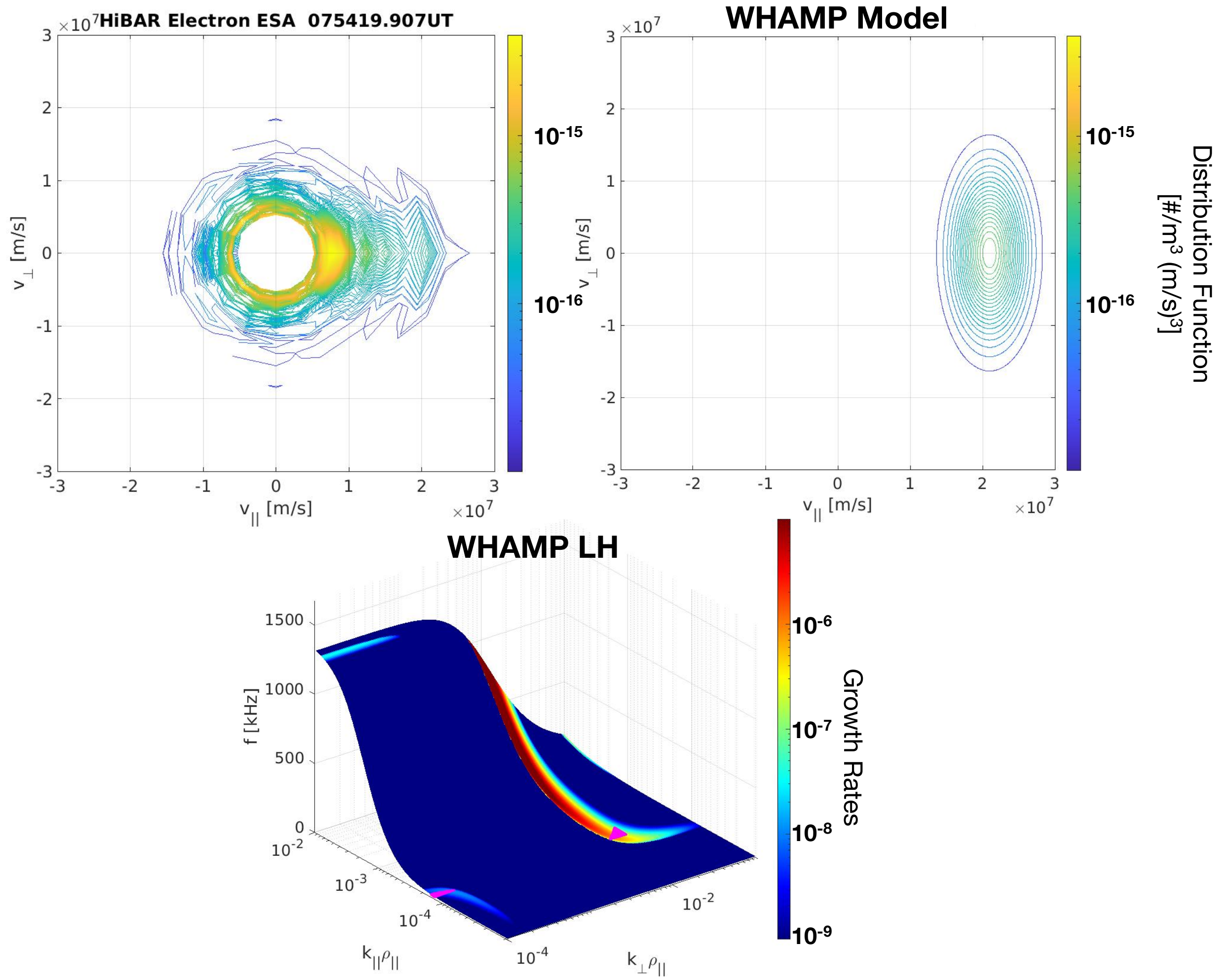

Figure 8. Measured electron distribution function from HIBAR's electron ESA data at 07:54:19.907 (top left) and model of the high energy beam seen in the measured distribution using a drifting Maxwellian (top right). The bottom panel shows the growth rates on the whistler/LH mode surface produced by the model WHAMP distribution along with the frequency and wavenumber matching conditions for the event labeled 260s in pink. The Langmuir/z mode surface showed no growth on the surface from this distribution.

Other possible sources of free energy are electrons above 20 keV and below 60 eV as well as the ions. Because the high and low energy electrons were not measured, they could not be modeled with WHAMP to find unstable features. As stated above, the instability that would be the source of the observed Langmuir waves may result from higher energy electrons than those that were measured. The ions were measured from 80 eV to 20 keV with a time resolution of 45 ms. In a similar analysis to that described above, the observed ion ring-like distribution at 09:54:19.920 UT was modeled using the WHAMP parameters, and growth rates on the whistler/LH modes were analyzed. The resulting model produced low growth rates on the surface $(< 10^{-7}$

Hz), but at wavevectors and frequencies that do not match those seen in Figure 7. Therefore, the ions are unlikely to be the source of these waves.

Another test of plausibility for a wave-wave interaction is to compare the electric energy density of the different waves to the thermal plasma energy density. The electric energy density, $\frac{1}{2}\epsilon_0 E^2$, for the plasma line is $\sim 10^{-21}$ J/m^3 and for the diffuse band is $\sim 10^{-23}$ J/m^3, 100 times smaller than that of the plasma line. The whistler/LH mode waves (likely dominated by whistler mode hiss) has an electric energy density of approximately 10^{-16} J/m^3. In comparison the plasma's thermal energy density is $nk_BT \approx 3 \times 10^{-9}$ J/m^3, where $n \sim 8 \times 10^4$ cm^{-3} is the plasma number density and $k_BT = 0.2$ eV is the typical auroral F-region temperature assumed for all events. The ratio of the electric to the thermal energy densities is $\sim 10^{-12}$ for the plasma line, 10^{-14} for the diffuse band, and 10^{-7} for the whistler/LH mode hiss. Because the diffuse feature is much weaker than the plasma line and the whistler/LH mode hiss, it suggests that the diffuse feature is a product of a wave-wave coalescence process ($W + L \rightarrow L'$) between the two others, the plasma line (L) and whistler/LH mode hiss (W). The whistler/LH mode energy density being much larger than the other two suggests that this is the primary driving wave, and the "plasma line" Langmuir waves are secondary, with the diffuse band being a product wave.

Incidentally, Akbari et al. [2013] observed double-peaked plasma lines in incoherent scatter radar data associated with strongly turbulent Langmuir cavitons. Although there is a superficial resemblance to the double-peaked plasma frequency spectra reported here, the extremely low ratio of electric to thermal energies in this case preclude an association with cavitons.

A more quantitative analysis is to examine the ratio of wave occupation numbers for these waves. The electric energy density is related to the plasmon occupation number through

$$\frac{1}{2}\epsilon_0 E^2 = \int \int_{k_{min}}^{k_{max}} \frac{2\pi k_\perp dk_\perp dk_{||}}{(2\pi)^3} \hbar\omega_i(\mathbf{k}) R_i(\mathbf{k}) N_i(\mathbf{k}) \tag{5}$$

where $R_i(\mathbf{k})$ is the ratio of the electric to total energy, $N_i(\mathbf{k})$ is the occupation number, and the volume integral is over the relevant region of wavevector space for a participating set of waves (e.g for the plasma line). The ratios $R_i(\mathbf{k})$, as determined by WHAMP, are approximately $\frac{1}{2}$ for both the plasma line and diffuse feature, and $\frac{1}{50}$ for the whistler mode hiss. For the plasma line combining this value of $R_i(\mathbf{k})$ with the electric energy density observed leads to a total energy density of approximately 2×10^{-21} J/m^3. The same procedure leads to total energy densities of 2×10^{-23} J/m^3 and 5×10^{-15} J/m^3 for the diffuse waves and the VLF whistlers, respectively.

Assuming the occupation numbers are the same for each wave mode, equation (5) can be rearranged and the ratios of occupation numbers determined to be

$$\frac{N_L}{N_W} = \frac{\frac{1}{2}\epsilon_0 E_L^2 \omega_W R_W \left[\int\int k_\perp dk_\perp dk_{||}\right]_W}{\frac{1}{2}\epsilon_0 E_W^2 \omega_L R_L \left[\int\int k_\perp dk_\perp dk_{||}\right]_L} \approx 8 \times 10^{-10} \frac{\left[\int\int k_\perp dk_\perp dk_{||}\right]_W}{\left[\int\int k_\perp dk_\perp dk_{||}\right]_L}. \tag{6}$$

The difficulty with solving this equation is determining the range of wavevectors that the modes occupy. To get a rough estimate of the ranges, the WHAMP surfaces are examined to determine possible ranges of wavenumbers for the observed waves and get an idea for the ratio of the occupation numbers. For the plasma line and diffuse feature, the broad range of wavevectors is $\rho_{||}k_{||} = 10^{-3} - 10^{-2}$ and $\rho_{||}k_{\perp} = 2 \times 10^{-4} - 2 \times 10^{-3}$. For the whistler/LH mode the wavevector range $\rho_{||}k_{||} = 10^{-4} - 10^{-2}$ and $\rho_{||}k_{\perp} = 2 \times 10^{-5} - 1 \times 10^{-4}$, where $\rho_{||}$ = 0.03 m. This covers the square patch of the surface where the different wave modes occur that match the conditions in Figure 7. Choosing these ranges in the wavevector integrals in equation (7) leads approximately to

$$\frac{N_L}{N_W} \approx 8 \times 10^{-10} \frac{2 \times 10^{-6}}{6 \times 10^{-4}} \approx 2 \times 10^{-11}. \tag{7}$$

Following a similar derivation for the time rate of change of the occupation numbers as in Moser et al. [2021], Cairns [1988], and Melrose [1980], among others, we can show that at saturation (when the rates of change of N_L and N_W are zero, ignoring linear growth and damping) the relationship of the whistler/LH mode occupation number to the Langmuir wave occupation numbers for the coalescence process is

$$N_W(N_L - N_{L'}) - N_L N_{L'} \simeq 0 \tag{8}$$

$$N_{L'} \simeq \frac{N_L N_W}{N_L + N_W}. \tag{9}$$

For each plasmon lost from the whistler/LH mode and the plasma line as the coalescence $L + W \rightarrow L'$ proceeds,, the diffuse mode gains one plasmon. From equation (9) the process saturates when

$$N_{Lo'} \approx \min(N_W, N_L). \tag{10}$$

This leads to a very small ratio of the Langmuir mode occupation numbers to the whistler/LH mode, with $N_{L'} \approx N_{Lo'} \approx N_L$ when $N_L \ll N_W$, which we've shown is the case from equation 7 for the observations.

Based on the foregoing observations and theoretical analyses it appears plausible that the diffuse band is formed by the nonlinear coalescence $L + W \rightarrow L'$ of whistler/LH mode waves W near the LH frequency with Langmuir waves L. The presumption is that the L and W waves are produced by distinct linear instabilities, most likely driven by an electron beam and/or by temperature anisotropies.

4 Conclusions

The HIBAR rocket was launched into active pre-midnight aurora and observed seven short duration bursts of Langmuir waves above the local plasma frequency at altitudes from 364-377 km. Of these seven events, five consisted of a plasma line at frequencies ranging from 2470–2610 kHz with an associated diffuse feature occurring 5–15 kHz above this line. Independent measurements of both the parallel and perpendicular components of the electric field showed that the plasma lines typically have $E_{||} \approx (2 \text{ to } 5)E_{\perp}$ and the diffuse features have $E_{||} \approx 2E_{\perp}$. These results are consistent with previous measurements of

Langmuir wave components, and are in line with theory, where waves in an overdense plasma above the plasma frequency experience Z-infinity resonance at angles with respect to the background magnetic field defined by equation (4). Using this equation with the plasma line and diffuse band frequencies shows that these waves would propagate at angles between 5–20°, which are comparable with the propagation angles produced by the $E_{||}/E_{\perp}$ ratio values using equation (3).

WHAMP was used to identify the Langmuir/z and whistler/LH surfaces where the plasma line and diffuse feature's wave modes would occur. The $E_{||}/E_{\perp}$ values are also consistent with the Langmuir/z surface at moderately oblique angles. Wavevector and frequency conservation for a 3-wave process involving the plasma line and diffuse band regions of the dispersion surface are consistent with the third wave being on the whistler/LH surface close to perpendicular propagation and with frequencies close to the LH frequency. The electron and ion data was used to determine instabilities on the LH surface and determined that the high energy electrons are the more likely source of these waves. The observed electric field energy densities of the whistler/LH waves are large enough, in comparison to the thermal energy density, for a nonlinear process to be viable. The wave energy densities decrease from the whistler/LH waves to the plasma line Langmuir waves to the diffuse band. Comparison of the different wave mode occupation numbers suggest the most plausible explanation is the coalescence of whistler/LH waves W with Langmuir waves L from the plasma line to produce the diffuse band of Langmuir waves L' via the process $W + L \rightarrow L'$. Both the W and L waves are believed to be produced by distinct linear instabilities.

This is similar to the process in Staciewicz et al. [1996], where observation of modulated Langmuir waves suggested these waves were produced through either parametric decay of the primary Langmuir wave into a LH wave and secondary Langmuir waves via the process $L \rightarrow L' + W$ or through the scattering of Langmuir waves off pre-existing LH waves via the process $L+W \rightarrow L'$, itself obviously a coalescence process. Bonnell at al. [1997] also presented a similar study of modulated Langmuir waves thought to be produced scattering off electrostatic whistler/LH waves, and showed this was the more likely process than the decay process in their situation. The observations presented here seem to be a similar process to these two studies, of a Langmuir/z mode wave coalescing with or scattering off of the whistler/LH, but here with the Langmuir/z mode waves having significantly weaker amplitudes.

Data availability. https://phi.physics.uiowa.edu/science/tau/data0/rocket/HIBAR_36200/

Author contributions. J.L. was the PI for the HiBAR mission. J.L. and C.M. interpreted the data and experiment. C.M. wrote the codes and performed the data analysis. I.C. contributed the theoretical analysis and all authors contributed to the interpretation of the results. C.M. wrote the manuscript with contributions from all authors.

Acknowledgements. Thanks to the team at Wallops Flight Facility and NASA for supporting the HIBAR payload and launch, as well as engineer Hank Harjes and NASA engineer Bill Payne for instrumentation support. Authors also thank S. Marilia, C. Feltmann, and S. Bounds for discussions and support. Research at Dartmouth College was supported by NASA grant NNX17AF92G.

References

Akbari, H., Semeter, J., Nicolls, M., Broughton, M., and LaBelle, J.: Localization of auroral Langmuir turbulence in thin layers, Journal of Geophysical Research: Space Physics, 118, 3576–3583, 2013.

Akbari, H., Labelle, J. W., and Newman, D. L.: Langmuir Turbulence in the Auroral Ionosphere: Origins and Effects, Frontiers in Astronomy and Space Sciences, 7, 116, 2021.

Beghin, C., Rauch, J., and Bosqued, J.: Electrostatic plasma waves and HF auroral hiss generated at low altitude, Journal of Geophysical Research: Space Physics, 94, 1359–1378, 1989.

Benson, R., Webb, P., Green, J., Carpenter, D., Sonwalkar, V., James, H., and Reinisch, B.: Active wave experiments in space plasmas: The Z mode, in: Geospace Electromagnetic Waves and Radiation, pp. 3–35, Springer, 2006.

Boehm, M., Carlson, C., McFadden, J., Clemmons, J., and Mozer, F.: High-resolution sounding rocket observations of large-amplitude Alfvén waves, Journal of Geophysical Research: Space Physics, 95, 12 157–12 171, 1990.

Bonnell, J., Kintner, P., Wahlund, J.-E., and Holtet, J.: Modulated langmuir waves: observations from freja and SCIFER, Journal of Geophysical Research: Space Physics, 102, 17 233–17 240, 1997.

Cairns, I.: Third and higher harmonic plasma emission due to Raman scattering, Journal of plasma physics, 38, 199–208, 1987.

Cairns, I.: A theory for the radiation at the third to fifth harmonics of the plasma frequency upstream from the Earth's bow shock, Journal of Geophysical Research: Space Physics, 93, 858–866, 1988.

Cairns, I. H. and Layden, A.: Kinematics of electrostatic 3-wave decay of generalized Langmuir waves in magnetized plasmas, Physics of Plasmas, 25, 082 309, 2018.

Chian, A.-L., Lopes, S., and Alves, M.: Generation of auroral whistler-mode radiation via nonlinear coupling of Langmuir waves and Alfvén waves, Astronomy and Astrophysics, 290, 1994.

Colpitts, C. and LaBelle, J.: Mode identification of whistler mode, Z-mode, and Langmuir/Upper Hybrid mode waves observed in an auroral sounding rocket experiment, Journal of Geophysical Research: Space Physics, 113, 2008.

Dombrowski, M., LaBelle, J., Rowland, D., Pfaff, R., and Kletzing, C.: Interpretation of vector electric field measurements of bursty Langmuir waves in the cusp, Journal of Geophysical Research: Space Physics, 117, 2012.

Ergun, R., Carlson, C., McFadden, J., Clemmons, J., and Boehm, M.: Langmuir wave growth and electron bunching: Results from a wave-particle correlator, Journal of Geophysical Research: Space Physics, 96, 225–238, 1991.

Ergun, R., Carlson, C., McFadden, J., Mozer, F., Muschietti, L., Roth, I., and Strangeway, R.: Debye-scale plasma structures associated with magnetic-field-aligned electric fields, Physical Review Letters, 81, 826, 1998.

Ergun, R., Malaspina, D., Cairns, I. H., Goldman, M., Newman, D., Robinson, P., Eriksson, S., Bougeret, J., Briand, C., Bale, S., et al.: Eigenmode structure in solar-wind Langmuir waves, Physical review letters, 101, 051 101, 2008.

Graham, D. B. and Cairns, I. H.: Electrostatic decay of Langmuir/z-mode waves in type III solar radio bursts, Journal of Geophysical Research: Space Physics, 118, 3968–3984, 2013.

Khotyaintsev, Y., Lizunov, G., and Stasiewicz, K.: Langmuir wave structures registered by FREJA: analysis and modeling, Advances in Space Research, 28, 1649–1654, 2001.

Kintner, P. M., Bonnell, J., Powell, S., Wahlund, J.-E., and Holback, B.: First results from the Freja HF snapshot receiver, Geophysical research letters, 22, 287–290, 1995.

LaBelle, J. and Treumann, R. A.: Auroral radio emissions, 1. Hisses, roars, and bursts, Space Science Reviews, 101, 295–440, 2002.

LaBelle, J., Cairns, I. H., and Kletzing, C.: Electric field statistics and modulation characteristics of bursty Langmuir waves observed in the cusp, Journal of Geophysical Research: Space Physics, 115, 2010.

Lizunov, G., Khotyaintsev, Y., and Stasiewicz, K.: Parametric decay to lower hybrid waves as a source of modulated Langmuir waves in the topside ionosphere, Journal of Geophysical Research: Space Physics, 106, 24 755–24 763, 2001.

Lopes, S. and Chian, A.-L.: A coherent nonlinear theory of auroral Langmuir-Alfven-whistler (LAW) events in the planetary magnetosphere., Astronomy and Astrophysics, 305, 669, 1996.

Lund, E. and LaBelle, J.: On the generation and propagation of auroral electromagnetic ion cyclotron waves, Journal of Geophysical Research: Space Physics, 102, 17 241–17 253, 1997.

Malaspina, D. and Ergun, R.: Observations of three-dimensional Langmuir wave structure, Journal of Geophysical Research: Space Physics, 113, 2008.

McAdams, K. and LaBelle, J.: Narrowband structure in HF waves above the electron plasma frequency in the auroral ionosphere, Geophysical research letters, 26, 1825–1828, 1999.

McAdams, K., LaBelle, J., Trimpi, M., Kintner, P., and Arnoldy, R.: Rocket observations of banded structure in waves near the Langmuir frequency in the auroral ionosphere, Journal of Geophysical Research: Space Physics, 104, 28 109–28 122, 1999.

McAdams, K., Ergun, R., and LaBelle, J.: HF chirps: Eigenmode trapping in density depletions, Geophysical research letters, 27, 321–324, 2000.

McFadden, J., Carlson, C., and Boehm, M.: High-frequency waves generated by auroral electrons, Journal of Geophysical Research: Space Physics, 91, 12 079–12 088, 1986.

Melrose, D.: Plasma Astrophysics, Vol. II, 1980.

Mende, S. B., Carlson, C., Frey, H., Immel, T., and Gérard, J.-C.: IMAGE FUV and in situ FAST particle observations of substorm aurorae, Journal of Geophysical Research: Space Physics, 108, 2003.

Moser, C., LaBelle, J., Roglans, R., Bonnell, J., Cairns, I., Feltman, C., Kletzing, C., Bounds, S., Sawyer, R., and Fuselier, S.: Modulated Upper-Hybrid Waves Coincident with Lower-Hybrid Waves in the Cusp, Journal of Geophysical Research: Space Physics, 2021.

Rönnmark, K.: WHAMP-Waves in homogeneous, anisotropic, multicomponent plasmas, Tech. rep., Kiruna Geofysiska Inst.(Sweden), 1982.

Samara, M. and LaBelle, J.: Structured waves near the plasma frequency observed in three auroral rocket flights, in: Annales Geophysicae, vol. 24, pp. 2911–2919, Copernicus GmbH, 2006.

Samara, M., LaBelle, J., Kletzing, C., and Bounds, S.: Rocket observations of structured upper hybrid waves at fuh= 2fce, Geophysical research letters, 31, 2004.

Schamel, H., Mandal, D., and Sharma, D.: Diversity of solitary electron holes operating with non-perturbative trapping, Physics of Plasmas, 27, 062 302, 2020.

Stasiewicz, K., Holback, B., Krasnoselskikh, V., Boehm, M., Boström, R., and Kintner, P.: Parametric instabilities of Langmuir waves observed by Freja, Journal of Geophysical Research: Space Physics, 101, 21 515–21 525, 1996.

Tsytovich, V.: Nonlinear effects in plasma, Plenum Press, new York, 1970.

Willes, A. and Cairns, I.: Generalized Langmuir waves in magnetized kinetic plasmas, Physics of Plasmas, 7, 3167–3180, 2000.